Characterization of Materials Report

Edward Deleu

Department of Electrical and Computer Engineering, Princeton University

MSE505, Characterization of Materials

Prof. Nan Yao

April, 19, 2025

Table of Contents

Confocal Microscopy 2

Scanning Electron Microscopy 5

X-Ray Diffraction 10

Transmission Electron Microscopy 12

Atomic Force Microscopy 15

Confocal Microscopy

Confocal microscopy is an optical imaging technique that implements laser-scanning functionality to precisely measure a sample's 3D topography. A confocal microscope is constructed with a pinhole at its detector such that it collects laser light from a single focal plane at a time, scanning over the z-height of a specimen to collect a full profile scan. The key feature enabling precise 3D imaging in confocal microscopy is the pinhole setup, filtering out-of-focus light allowing for precise optical sectioning. The confocal pinhole only allows for the collection of in-focus light at each optical section. The Keyence VK-X3050 3D laser-scanning confocal microscope is used for imaging in this report which also has optical functionality to add color information to scans. This microscope is equipped with objective lenses of various magnifications (10x, 20x, 50x, etc.) so that various magnifications may be obtained as well as finer z-resolution with the higher magnifications. The system is equipped with a $661nm$ red laser.

To use the Keyence laser confocal microscope, a butterfly-wing sample affixed on a glass slide is placed on the microscope's stage—no other sample preparation is necessary. The z-height of the stage is adjusted to optically bring the sample into focus, followed by fine-tuning through the microscope's autofocus functionality. At a low magnification (10x), a "navigation" image may be created to get an overview of the sample and allow for simple x-y navigation using the software interface. An interesting site on the sample is then chosen for imaging and the confocal z-scan is performed.

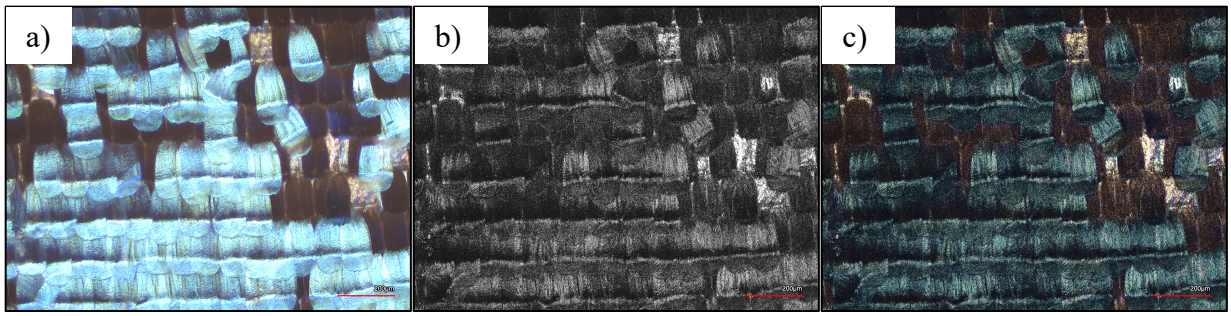

Figure 1: Confocal microscope images at 10x of a butterfly-wing sample (scale bar: $200\mu m$*). (a) The optical image. (b) The laser scan image. (c) The combined image with both optical and laser components overlaid.*

Fig. (1) demonstrates the set of images collected from the 10x laser confocal scan. The microscope produces separate optical and laser images, as well as a combined view which helps discern some depth and texture information while maintaining the color of the original sample. This color information can be helpful to orient and understand a sample beyond the grayscale scan. The contrast in the grayscale laser scan corresponds to variations in reflected laser intensity across the sample surface. The image is produced by combining the individual z-scans into a single image: at each lateral (x, y) position in the image, the brightness corresponds to the maximum signal across the entire range of z-scans. The contrast provides surface texture, although the exact 3D structure is lost in this image; still, this is a meaningful way to view a projection of the sample's topography and texture. This set of images shows that the butterfly-wing is made up of small scales organized in overlapping rows. It is also apparent that the sample has been disturbed and the scales on the right side of the image have been displaced and moved around. This is clear from the combined image where there are dark spots, indicating that the area has a lower z-height than the surrounding scales. While these images give a good

overview of the sample, it is still hard to discern exact height information. The software packaged with the microscope also produces height maps which demonstrate the utility of the confocal microscope.

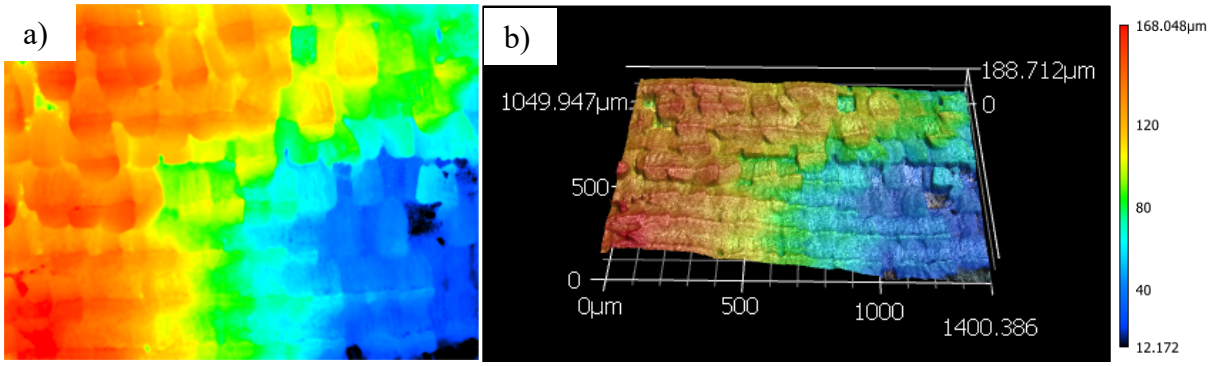

Figure 2: Confocal microscope height maps at 10x of a butterfly wing sample. The section in view is $1.40mm \times 1.05mm$*. (a) Pseudocolor 2D height map of the wing's surface. (b) 3D reconstruction of the wing surface, pseudocolor-coded for height.*

Fig. (2) displays a heatmap view of the butterfly-wing's height, as both a 2D image and corresponding 3D plot. The left side of the sample is higher than the right side, perhaps due to the entire sample being warped. The height map indicates that there is approximately $150\mu m$ of elevation change within this region of the sample. This height map also shows how the scales are layered on top of one another, organized in rows. Small horizontal ridges are seen where scales overlap one another, at the locations where the below layer of scales terminate.

A laser confocal scan is also performed at a magnification of 50x, producing similar data as before. This higher magnification allows for a finer resolution with the tradeoff of a slower data-collection process. This allows for more detailed analysis of the ridges and nanostructure of the butterfly wing.

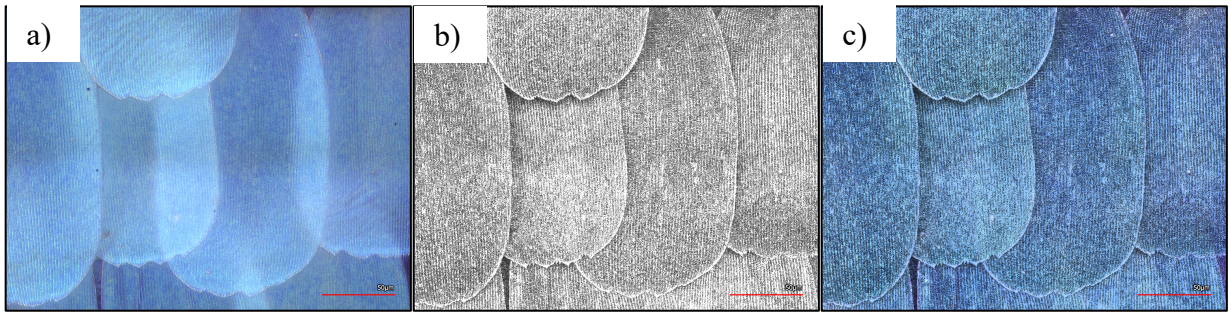

Figure 3: Confocal microscope images at 50x of a butterfly wing sample (scale bar: $50\mu m$*). (a) The purely optical image. (b) The laser height map. (c) The combined image with both optical and laser information overlaid.*

Fig. (3) presents a clear view of the individual scales. In the optical image, the scales appear as semi-translucent and the regions where the scales overlap one another can be seen. This results from the penetration of light through the very thin scales. The laser and combined images do not depict this translucency and instead are more refined views of the surface of the scales and the texture. The scales appear to have vertical splines that are closely spaced together, running along the entire length of each scale. The scales are not entirely uniform: the tips of each scale are a bit jagged. Some of these splines also overhang the jagged tips of the scales.

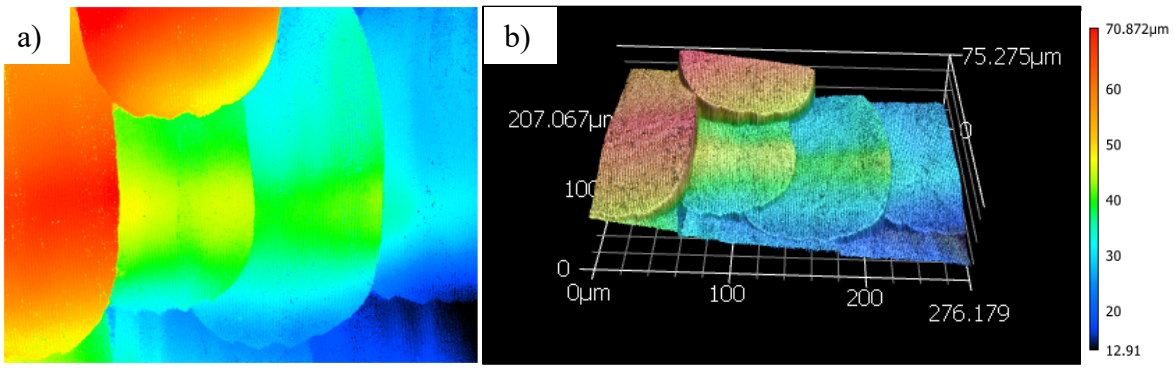

Figure 4: Confocal microscope height maps at 50x of a butterfly wing sample. The section in view is $276\mu m \times 207\mu m$
(a) Pseudocolor 2D height map of the wing's surface. (b) 3D reconstruction of the wing surface, pseudocolor-coded for height.

The height maps in Fig. (4) neatly depict the overlapping of the scales, as well as the vertical splines which are clear in both the 2D and 3D representations. Since the scales are each at distinct z-heights, the color-coded 2D height map also neatly outlines the edges of the individual scales which have quite uniform size and shape. This scan again confirms that the left-side of the sample appears to be elevated compared to the right-side: this scan has an elevation change of approximately $60\mu m$ from the lowest to highest points. Compared to the height maps in Fig. (2), these display a significantly smaller region of the sample while maintaining a very fine resolution and precise z-information. It is much easier to resolve small details about the butterfly-wing sample in this scan, as a result of the improved z-resolution and magnified view.

Scanning Electron Microscopy

A scanning electron microscope (SEM) utilizes electrons, rather than electromagnetic radiation, to image a sample. An electron gun under high-vacuum conditions produces a high-power beam that passes through a series of lenses and magnetic coils to produce a highly focused beam focused on the sample. Using magnetic scanning coils, the SEM precisely scans the beam across the sample to collect data over a desired region. The concentrated electron beam interacts with the individual atoms of the sample in different ways, and different detectors may be used to collect various information. Backscattered electrons are high energy electrons that reflect off the atomic nuclei and are useful for determining density and crystallographic information. Secondary electrons are electrons that are emitted from the surface of the sample: they are low energy valence electrons that have been knocked off due to the incident high-energy beam. A forward-biased secondary electron-detector is used for the imaging in this report.



Figure 5: FEI Quanta 200 SEM

Typically, high vacuum is required to collect SEM images so that there is no contamination of the field emission gun and to minimize scattering of the beam besides at the sample. However, samples for imaging must be conductive and grounded so that charge does not build up on the sample's surface which may cause unwanted artifacts and distortions. This poses an issue since the butterfly-wing sample is non-conductive. To mitigate charging artifacts, the butterfly-wing samples are lightly sputtered with a 15nm conductive coating of Iridium using an ion beam sputterer. This alone may not entirely be sufficient for clear imaging: additionally, the FEI Quanta 200 SEM pictured in Fig. (5) allows for low-vacuum and environmental (ESEM) imaging modes. To image the butterfly-wing sample, the SEM is set to low-vacuum mode with a chamber pressure of $0.45\ \mathrm{Torr}$ and the introduction of H_2O gas to improve the imaging quality. When these H_2O molecules are positively ionized by electrons, they can effectively neutralize the charge build up on the sample's surface. This allows for a stable and clear imaging process without any undesirable artifacts. Secondary electrons released from the water vapor may also effectively amplify the signal from the sample's surface. The field emission gun is maintained at high vacuum with pressure-limiting apertures, ensuring beam quality.

The sputtered butterfly-wing sample is attached to an Aluminum-stub compatible with the SEM sample holder such that there is electrical contact between the stub and sample coating. Once the sample is placed within the SEM, vacuum must be accomplished in the chamber and upper column. The gun reaches a pressure of $9.41 \times 10^{-10}\ \mathrm{Torr}$ and the chamber reaches $0.450\ \mathrm{Torr}$. The height of the sample must also be adjusted to approximately a 10mm working distance: this distance is a good trade-off between resolution and depth-of-field. The beam power must then be set, depending on the desired resolution. The beam power is set to 5kV to achieve good surface clarity. Low kV settings are good for surface imaging due to having relatively shallow interaction volumes, as well as being suitable for non-conducting samples. The beam may then be turned on and the sample may be navigated at low magnification. Once a suitable area is found, the magnification is set to $> 30{,}000x$ for focusing. In addition to focusing, the astigmatism in the beam must be corrected by using the x and y stigmators. This fine-tuning step is crucial, going back and forth between stigmating and focusing. Sometimes, a lens alignment step is also required to obtain a steady image.

Fig. (6) depicts the butterfly-wing sample imaged with the SEM setup described above at a magnification of 475x. SEM images are typically shown in grayscale since the pixels represent the relative intensities of secondary electrons at the respective sample locations. To obtain this image, the electron beam focuses on each site for 100µs. Faster dwell-times are also possible, but they produce noisier images. The image is visually much more detailed compared to the confocal images: very fine details on the butterfly-wing scales can be seen. The scales appear to be covered in a network of small rectangular cells that are longer in the vertical direction. While the vertical splines were clear in the confocal images, the small horizontal cell-like connections between splines were not previously clear. This texture appears to be disturbed on many of the scales, leaving areas of smoothness, but the top and middle rows of scales appear to be mostly intact compared to the large bottom-left scale that is missing the network on its right half. The splines can also be seen littering the left and bottom of the image where the scales are missing. As in the confocal images, the vertical splines slightly extend beyond the body of the scales. The attachment point of the scales can be seen in the position of the top row where there is a missing scale: the scales look to be attached with a small oval-shaped stem that extend into the body of the wing.

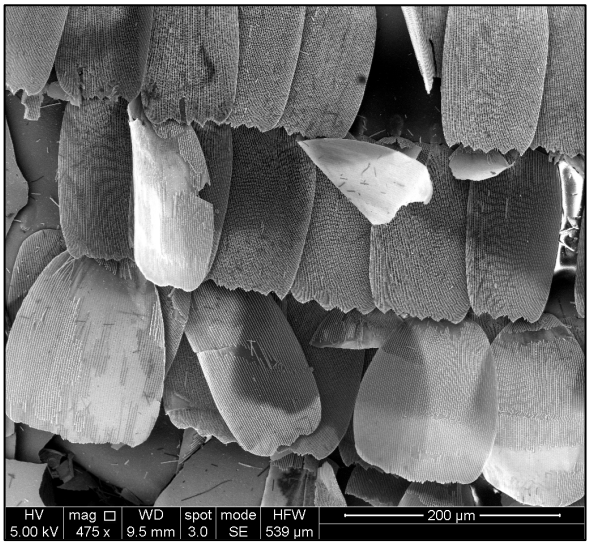

Figure 6: SEM image of butterfly-wing sample captured in low-vacuum at 475x magnification, 5kV power, and a 100µs dwell time. The fine cell-like surface details are resolved, and damaged areas of the scales are also evident.

Fig. (7) displays the same sample at much higher magnification, demonstrating the very versatile nature of the SEM. The horizontal width of the image has been reduced from $539\ \mu\text{m}$ to just $7.24\ \mu\text{m}$. The SEM is zoomed in on one of the pointed tips of the scales, displaying very clearly its structure. At this scale, the splines actually overlap one another in the vertical direction. Between the individual stacks of splines, there are also irregularly spaced horizontal connections– this was the cell-like network seen at lower magnification. In the background of the image, which is slightly out of focus due to the limited depth-of-focus of the SEM, the same periodic grid structure is seen on the surface of another scale.

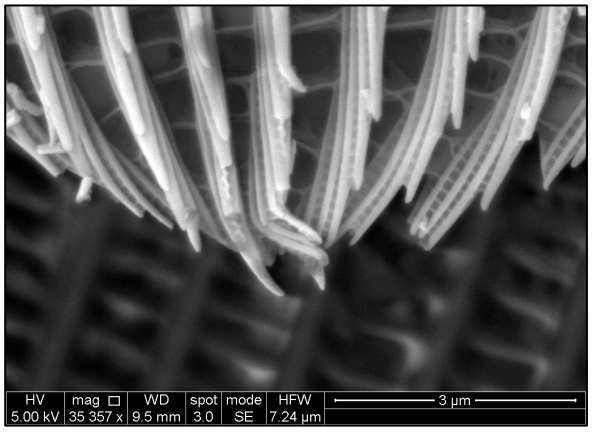

Figure 7: SEM image of butterfly-wing sample, focused on the tip of a scale, captured in low-vacuum at 35,357x magnification, 5kV power, and a 100µs dwell time.

Scanning electron microscopes also have additional functionality that is useful for determining compositional information about a sample through characteristic x-rays, utilizing Energy Dispersive X-ray Spectroscopy (EDXS) or (EDX) for short.

As before, a SEM image may be collected with the secondary electron detector. The same fundamental setup and focusing steps are necessary for performing EDX analysis. The incident electron beam may eject an inner-shell electron to create a vacancy. When higher-shell electrons fill the vacancy, they must release energy to transition: this results in the release of characteristic x-rays. A common transition is termed "$K\alpha$" and is where an electron falls from the L shell to fill a vacancy in the K shell, releasing the corresponding $K\alpha$ x-ray. The electron beam energy level is critical, since each element has distinct x-ray emission characteristics at certain energy levels. Thus, the electron beam must have sufficient energy to eject the inner-shell electrons of the given sample. If an element, say copper, has a $K\alpha$ energy of $8.04\ keV$, the beam energy should be set approximately 150% this value, say $12\ keV$. There are various possible transitions, so each element may have characteristic x-rays at multiple energy levels which will show up as multiple peaks on the resulting spectrum. Some elements will only show up on the spectrum at higher kV, which will correspondingly require a higher power electron beam. If the elemental composition is completely unknown, setting a high kV beam power is required. This also increases the interaction volume, so it is not desirable in all situations. The detector has a resolution of approximately 130eV and cannot precisely distinguish different x-rays of energies within this amount of separation.

For the butterfly-wing sample, an electron beam voltage of 10kV is chosen since the exact elemental composition is unknown and this should provide for a safe margin for the expected carbon, oxygen, and other light elements. In theory, this setup should have capabilities to detect elements approximately up to germanium on the periodic table. For analysis, the SEM is focused on a particle-like defect to determine its composition, as well as the composition of the butterfly-wing itself. As before, the SEM is set to low-vacuum mode with a spot-size of 3, this time with a chamber pressure of $0.30\ \text{Torr}$. The resulting SEM image is pictured in Fig. (8) at $12{,}946x$ magnification. The unknown particle is resting on a scale of the wing, comprised of the grid-like network seen in the background of Fig. (7). This image also confirms that the vertical splines are stacked upon each other.

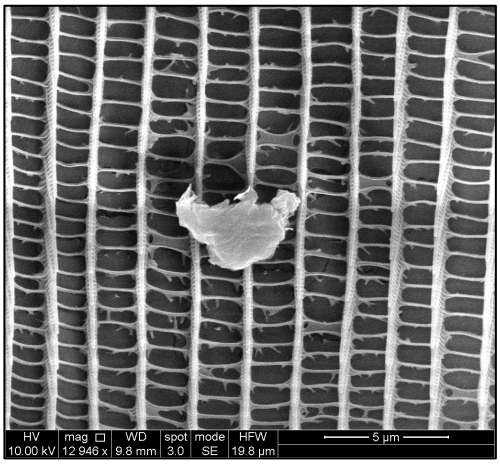

Figure 8: SEM image of the butterfly-wing sample, focused on an unknown particle, captured in low-vacuum at 12,946x magnification, 10kV power, and a 3µs dwell time.

This setup yields a reasonable EDX input count rate of approximately $3{,}500\ \text{cps}$ and an output count rate of approximately $3{,}000\ \text{cps}$; if the count rates are too low, spot size may be increased to collect a larger signal strength. In the Aztec software, information about the sputtered $\approx 15nm$ Iridium coating is entered so that it is excluded from the sample's elemental composition.

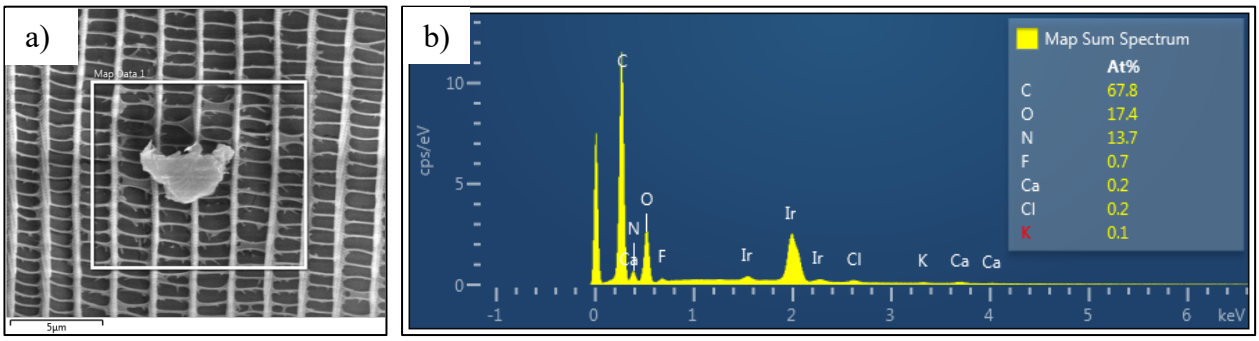

Figure 9: EDXS analysis of an unknown particle on the butterfly-wing sample. (a) SEM image of the butterfly-wing sample with a bounding box for the EDS analysis. Captured in low-vacuum at 12,946x magnification and 10kV power. (b) EDXS spectrum of the bounded region displaying relative intensities of detected x-ray energies, highlighting the region's elemental composition.

A rectangular region of the sample is chosen to analyze, pictured in Fig. (9a). The EDS analysis is performed over the bounded region to determine the composition of the unknown particle, displayed in Fig. (9b). The EDS analysis yields a spectrum plot, displaying relative intensities vs. energies for the detected characteristic x-rays. The Aztec software maps the intensity peaks to different elements based on their known electron transitions. Since the spectrum is essentially empty from 5 to 10 keV, this indicates that the desired beam power is sufficient and no higher Z elements are present in detectable quantities. The analysis displays the relative atomic percentages of the different elements detected in the region. However, these percentages should not be taken as entirely robust since these are only the percentages of the few elements detected from this small, non-uniform region. Furthermore, this method is limited in detecting trace amounts of elements. Still, this indicates that the composition over the region is predominantly carbon. The peak at 0keV is an artifact due to the noise level and is used for calibration.

The EDS analysis also yields elemental maps which are crucial in understanding the spectrum and distinguishing between the wing itself and the unknown particle. These elemental maps are displayed in Fig. (10) for the 8 distinct elements detected in the bounding box.

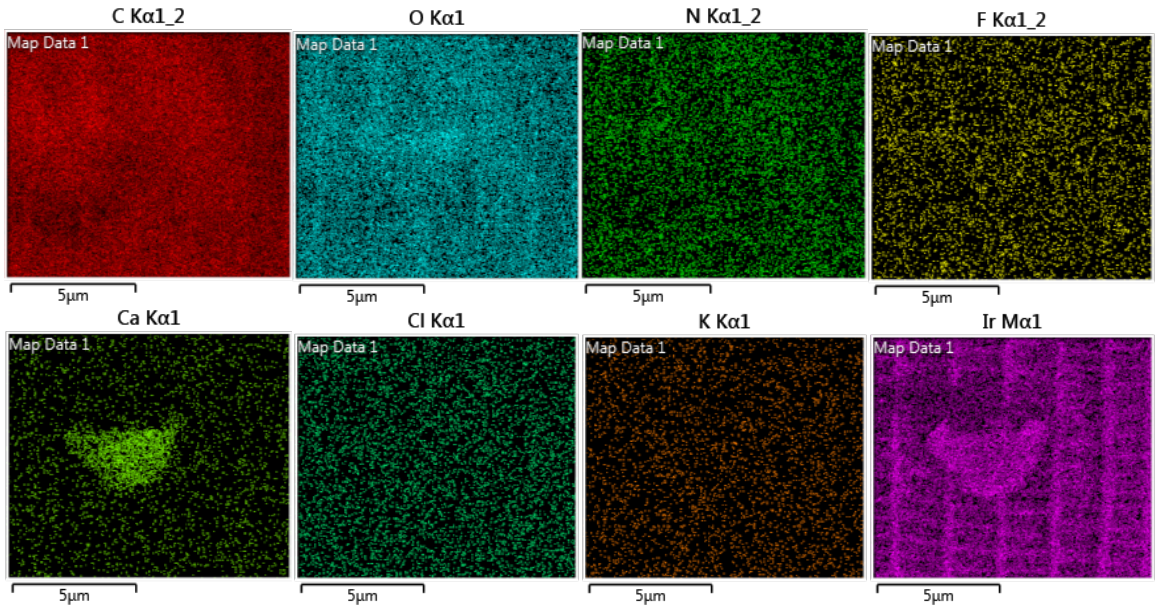

Figure 10: EDS elemental maps of an unknown particle on the butterfly-wing sample for the 8 elements detected in the spectrum.

Each element is presented in a distinct color, and each colored pixel represents characteristic x-rays detected from that location within the bounding box for the corresponding element. The relative frequency of colored pixels corresponds to the intensity of the detected signal. The elemental map for Iridium nicely depicts the topography of the sample, demonstrating that it relatively uniformly coated the entire sample including the unknown particle. In Fig. (9b), Iridium is excluded in the atomic percentages of elements as specified in the software.

The maps for carbon, oxygen, and nitrogen indicate that these elements are evenly dispersed throughout the butterfly-wing sample. In combination with the information in Fig. (9b), this indicates that the sample is mostly composed of Carbon, with smaller amounts of Oxygen and Nitrogen. Trace amounts of fluorine, chlorine, and potassium are also detected throughout the entire sample. The red lettering for K in Fig. (9b) indicates that the software is not confident in the presence of potassium and that this may simply be a spurious detection due to noise.

The map for calcium in Fig. (10) depicts a high density of points at the unknown particle, clearly outlining its shape. The density of points away from the unknown particle is significantly lower. This serves as evidence that the unknown particle is a small piece of calcium, perhaps with trace amounts of other elements. Since the elemental maps for the other elements are relatively uniform, this indicates that the characteristic x-rays are penetrating through the particle and revealing information about the butterfly-wing's scale rather than the particle itself.

X-Ray Diffraction

In contrast with scanning electron microscopy, x-ray diffraction (XRD) utilizes x-rays produced by an x-ray tube to probe structural information from a sample. These x-rays are generated in an x-ray tube where electrons are accelerated at an anode target which then emits characteristic x-rays. In the case of XRD, a copper anode is used which has a $K\alpha$ characteristic x-ray with a de Broglie wavelength of 1.54 Å. In essence, these x-rays are generated by the same mechanism as in EDXS, but they are now being used as a source to probe crystallographic information.

These x-rays filter through a network of optics for focusing and collimating, hitting a sample from an angle θ. When the x-rays collide with the sample, they will be scattered by the electron clouds surrounding the atoms. Interference is possible since the x-ray wavelength 1.54 Å is comparable to the interatomic separation between the atoms. Constructive interference occurs according to Bragg's Law, $n\lambda = 2d_{hkl}\sin\theta$. In a single-crystalline sample, an interference maximum will appear associated with a specific set of atomic planes (separated by a distance d_{hkl}) and an associated angle θ. In a polycrystalline or powdered sample, there exist many crystallites in random orientations. Incident x-rays will then diffract with all sets of atomic planes, leading to diffraction peaks at various angles. An XRD experiment utilizing a powdered substance is aptly termed a "Powder Diffraction" and is followed in this report.

Bragg's Law serves as the basis for XRD measurements which follow a "$\theta - 2\theta$ Experiment". The angle θ is the incident angle between the sample and x-ray source, and the angle 2θ is then formed between the x-ray beam and the detector. When the x-ray source and detector are constrained according to this relationship, the Bragg geometry is enforced, and the detector will collect the intensity of the diffracted x-rays due to the crystal diffraction. The angle θ is slowly varied through a range of approximately $0 - 45°$ to find the interference maxima and their relative intensities for a given sample. By interpreting the resulting spectrum, one may determine the crystal structure and even the elemental composition of a sample.

An unknown powdered sample is prepared on a glass slide, secured with plastic cling-wrap, and is securely attached to the stage of the Bruker Discover D8 x-ray diffractometer using double-sided tape. After appropriate calibrations of the apparatus and alignment of the sample, a $\theta - 2\theta$ experiment is performed within the 2θ range of $20° - 80°$ at a speed of $10°/\text{minute}$ and a step size of $0.05°$. This angular range is appropriate since it corresponds to interplanar spacings between approximately $[1.2, 4.5]$ Å which is reasonable for most samples. The resulting spectrum is presented in Fig. (11). Each intensity peak corresponds to diffraction from a specific

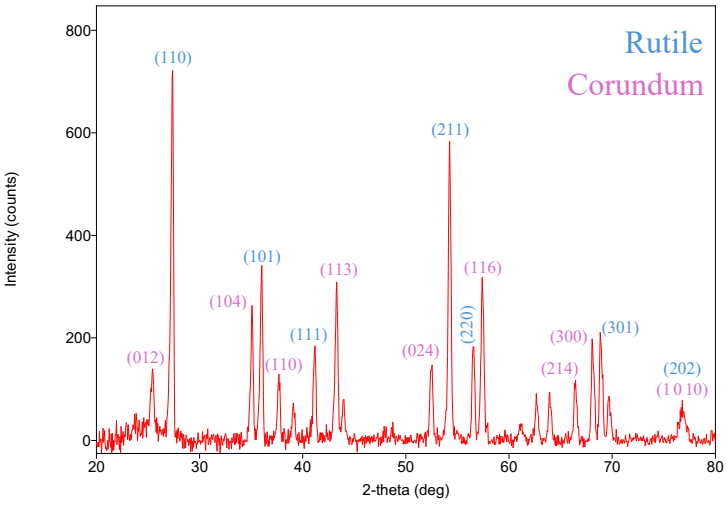

Figure 11: X-ray diffraction spectrum displaying the relative intensity of detected x-rays as a function of angle 2θ for the unknown powdered sample. Miller indices from the most prominent peaks have also been annotated for the two constituent materials.

set of atomic planes. The amplitudes are simply the counts of x-rays detected at each given angle. These amplitudes are influenced by the geometric structure factor of a crystal structure, which directly relates to the arrangement of atoms and their electrons.

This diffraction spectrum is then imported to the PDXL2 software which analyzes the relative intensities, locations, and widths against a large database, finding the most promising candidate structures. According to the analysis software, the unknown specimen is comprised of a mixture of two distinct synthetically formed powders, Rutile (TiO_2) and Corundum (Al_2O_3) aka ruby. Both matches yield low Figures of Merit (FOM) below 0.32, indicating a high-quality match to the reference spectra. The software matched over 20 peaks, with interplanar spacings between $[1.24, 3.49]$ Å and crystallite sizes estimated between $[200, 335]$ Å by fitting the width of the peaks. This analysis also provides an estimate of the ratio between these substances using the Reference Intensity Ratio (RIR) method which utilizes a ratio of strongest peak intensities. According to this analysis, the sample contains 40 wt% rutile and 60 wt% ruby.

Datasheets of the constituent substances are also provided which may help to identify the specific crystal structures and parameters, as well as the exact crystal planes and their spacings that x-rays are diffracting from. Rutile is part of the tetragonal crystal system with the 136 space group; its lattice parameters are $a = b = 4.5933$ Å, $c = 2.9592$ Å. Corundum is hexagonal with the 167 space group; its lattice parameters are $a = b = 4.7657$ Å, $c = 13.01$Å. The reference diffraction spectra are depicted in Fig. (12), with some of the most prominent diffraction peaks labeled with the corresponding set of diffracting planes. For example, rutile's diffraction peak at $2\theta = 27.45°$ corresponds to an interplanar spacing of 3.247 Å between the (110) planes. The most prominent peak in Fig. (11) is at $27.41°$, indicating that this is from the rutile (110) planes with an estimated crystallite size of 300 Å. Another peak is at $35.13°$ which corresponds to ruby's (104) set of planes with a spacing of 2.555 Å and estimated crystallite size of 298 Å. In-essence, the PDXL2 software analyzes the collected peaks and matches them to the reference spectra. Since the sample is a mixture of the two substances, the overall diffraction spectrum in Fig. (11) is a scaled superposition of the two spectra in Fig. (12).

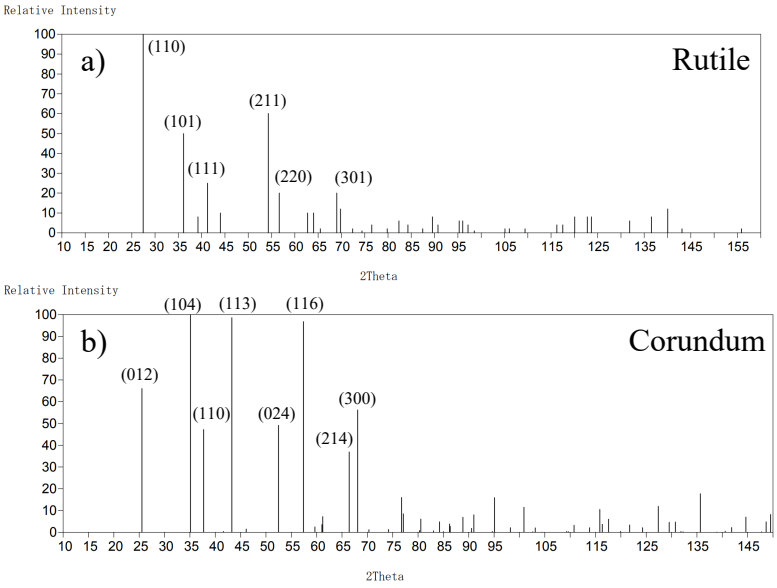

Figure 12: Reference x-ray diffraction spectra of Rutile and Corundum with annotated miller indices for the most prominent peaks. a) Reference spectrum for synthetic rutile. b) Reference spectrum for synthetic corundum.

Some of the most prominent peaks in Fig. (11) have also been labeled according to the corresponding substance and planes from the reference spectra. These planar assignments confirm PDXL2's match and demonstrate the power of utilizing powder diffraction to identify unknown crystalline samples, even when a mixture is present.

Transmission Electron Microscopy

Transmission electron microscopy operates on similar principles as scanning electron microscopy. A transmission electron microscope (TEM) also uses a beam of electrons and a series of electromagnetic lenses to focus the electron beam on a specimen. With SEMs, electrons and x-rays originating from the surface of the sample are collected. In contrast, the electron beam in TEMs passes through a thin sample. The transmitted electrons then pass through a series of optics and apertures, depending on the imaging mode. TEMs may operate in either diffraction or projection mode: diffraction allows for the viewing of the reciprocal-space diffraction pattern, while projection mode allows for the viewing of the real-space image. After passing through the optics, electrons collide with a fluorescent screen which captures the transmitted electron information. TEMs are powerful for imaging and understanding the structure of a sample at an extremely high resolution, rather than simply capturing surface characteristics as with SEMs.

In standard bright-field imaging, electrons pass through the objective-lens and then a centered aperture. In the resulting images, bright spots indicate areas where the electron beam most easily passed through the sample. Dark spots indicate areas where the electron beam collided with the sample and scattered most significantly with the sample's electrons. For example, thicker regions of a sample or regions with a higher atomic number Z will appear darker in the resulting TEM image. This contrast is known as mass-thickness contrast. In general, TEM samples must be extremely thin such that the electron beam may easily pass through.

The FEI Talos L120C TEM seen in Fig. (13) is used for imaging in this report. A standard sample is imaged that has sputtered gold particles on a thin support film of amorphous carbon. These gold-particles have been patterned on a standard carbon-coated copper TEM grid – the metal grid is used as structural support for TEM samples. Drop-casted polystyrene particles are also present on the sample. The mesh of the sample is held in place on a single-tilt sample holder. At lower magnifications, this grid-pattern can be seen in the TEM images overlaid on the specimen.



Figure 13: An image of the FEI Talos L120C TEM.

Once all alignment and calibration steps are completed, the TEM is ready for imaging. At a given magnification, the intensity of the electron beam should be adjusted such that the circular electron beam just illuminates the entire square viewing frame. These adjustments are accomplished through the adjustment of the probe size with the condenser lenses. Then, the focus must be carefully adjusted to achieve the minimum contrast condition where there are no bright or dark outlines or fringe effects on the outlines of the specimen. The image may slightly be defocused to achieve slightly better contrast and a more appealing image. The electron beam remains in a single spot for TEM imaging, as opposed to SEMs which scanned the electron beam across the specimen to form an image.

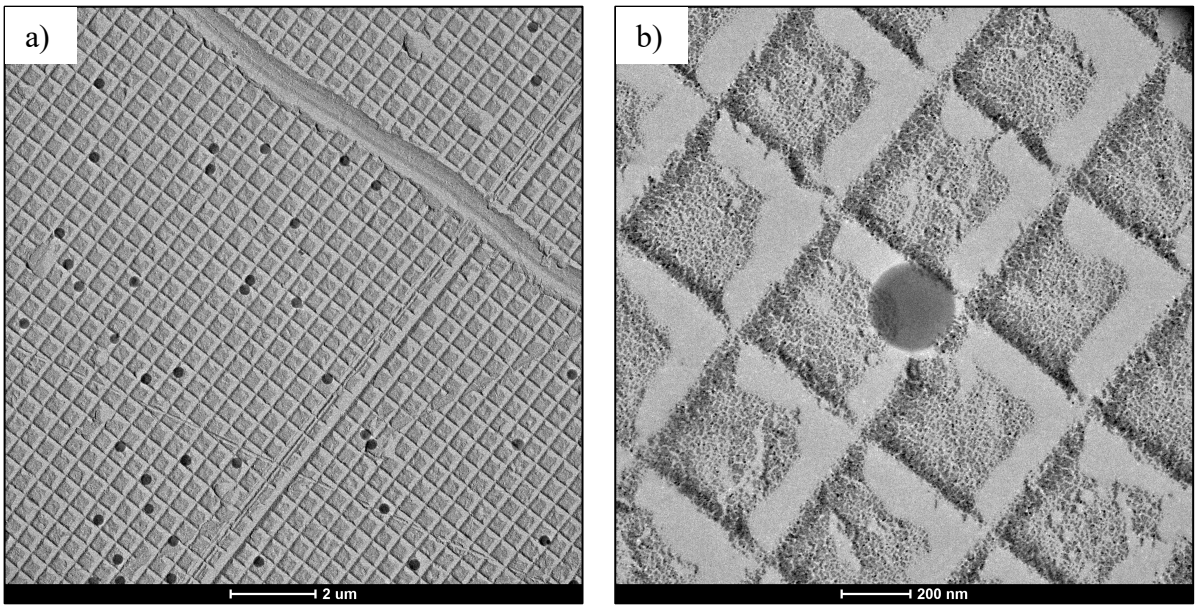

Figure 14: Bright-field TEM image of a standard specimen focused on a patterned region of gold with dispersed polystyrene particles at 120kV, captured at (a) 3,400x magnification and (b) at 36,000x magnification.

Fig. (14) displays two TEM images of the sample, gold particles sputtered on an amorphous carbon film with sparsely distributed polystyrene particles. Fig. (14a) depicts the sample at 3,400x magnification: the irregularly distributed black circles are polystyrene nanospheres, and the repeating grid structure is gold particles sputtered in a pattern of squares. Narrow gaps separate each gold square. The bulk of the sample is light gray, representing the uniform bulk thin film of carbon which the electron beam easily passes through. The sputtered gold particles are individually small black dots in Fig. (14a) that are clustered together to form the regularly sized squares. This sample can be used for calibration: the side-length of the squares is generally known, and this can thereby be used to calibrate the scale in the TEM. The left and bottom sides of these squares are a bit darker, indicating a higher density of the gold particles along these grid edges. There are some macroscopic scratches and defects interrupting the periodic grid structure at random angles, perhaps from mishandling of the sample. The most noticeable defect is the scratch running at an approximately $45°$ angle in the upper right section of the image with a width around $0.5\ \mu\text{m}$.

Fig. (14b) depicts the sample at higher magnification, 36,000x. The image is centered on a polystyrene particle which appears as a relatively uniform black circle, about 200nm in diameter. Moving radially towards the edges of the circle, the brightness slightly decreases, indicating that the particle is thickest at its center. This supports that the polystyrene particles are spherically shaped. This image provides a much better view of the sputtered-on gold squares. Each square is separated on the grid with reasonably sized gaps, indicated by the blank gray regions of amorphous carbon. Each gold square has a uniform shape and size, and it appears that thin lines of gold particles connect most squares at their lower and leftmost edges. The lower and leftmost edges of each square are again seen to be darker, indicting slightly higher density of gold particles. Within the squares of gold, there are some blank gray areas indicating an absence of gold-particles. The gold particles within the squares vary in thickness and density, indicated by

the variance in the darkness of the particles from lighter to darker grays. The darkest pixels likely indicate where gold particles overlap one another.

Fig. (15) presents yet another magnified view of the same sample, this time at 310,000x. The lower region of the image is filled by the upper half of a polystyrene sphere. The upper region of the image is a square of the gold particles, and the left-side of the image is a gap in the grid. At this scale, it is clear that the polystyrene particle becomes lighter moving radially outwards towards it edge. The outer edge of the sphere has some lightly colored pixels, indicating a lower thickness here. The polystyrene particle overlaps the gold in the right side of the image: the gold particles can vaguely be seen underneath the circle. This demonstrates the power of TEM to penetrate through a specimen to reveal information about its structure and layers.

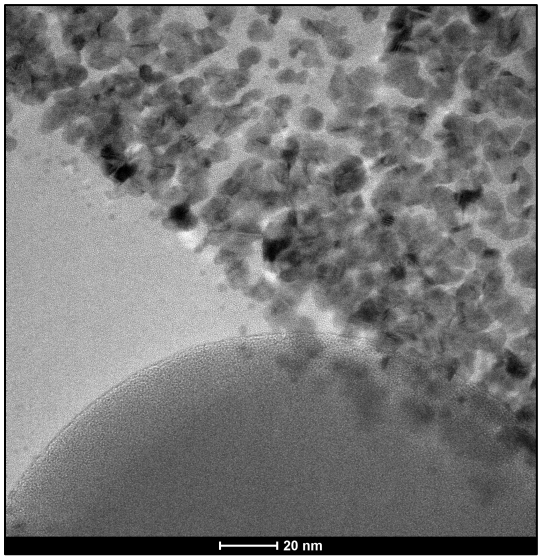

Figure 15: Bright-field TEM image of standard specimen focused on a patterned region of gold with a Polystyrene particle at 120kV, captured 310,000x magnification.

The gold particles themselves appear as quasi-spherical and amorphous with a distribution of sizes roughly in the 5-15nm range. The particles are spaced much more closely together at this bottom edge of the square. There are also some black spots where the sputtered gold particles are stacked on one another. The gap region appears with constant contrast, indicating that there are no other visible impurities or particles on the carbon film.

These TEM images demonstrate the technique's great ability to resolve sample details and morphology with nanoscale resolution.

Atomic Force Microscopy

Atomic force microscopy is a versatile type of scanning-probe microscopy, utilizing a cantilevered probe to discern surface information about a sample. In its most basic form, this is a great method to collect topographic information about a sample with minimal sample preparation. An atomic force microscope (AFM) scans a sharp tip over the surface of a sample, point-by-point, to create a surface map. A laser is reflected off the backside of the cantilevered probe: probe-movements are consequently determined by the position of the laser's reflection incident on a photodetector. An AFM typically has a vertical resolution < 0.05 nm and a lateral resolution around $1 - 5$ nm.

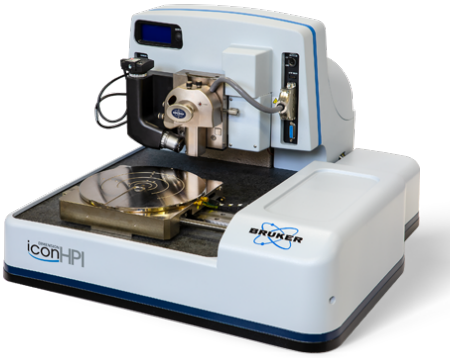

Figure 16: A photograph of the Bruker ICON series Atomic Force Microscope (AFM).

Depending on the probe-used, an AFM can collect various kinds of information about a sample; for example, magnetic properties, electrical properties, surface elasticity, or even surface adhesion to name a few. For this report, topographic height information is collected with the Bruker ICON3 AFM, operated in tapping-mode. In this operation mode, the cantilever is oscillated near its resonant frequency so that the tip repeatedly taps on the sample as the probe scans over the surface. A feedback loop attempts to maintain a constant oscillation amplitude: the vertical height of the probe is collected such that a topographic map of the surface is created. An "error-image" can be collected which may offer enhanced contrast and detail: this depicts the error between the set amplitude and measured oscillation amplitude, representing the error in the feedback loop. In tapping mode, a "phase-image" may also be created which corresponds to the relative phase-differences of the probe's driven and actual oscillation frequency as it scans over the sample. Other operation modes include contact-mode where the tip is simply dragged across the sample's surface and non-contact mode where the probe experiences deflection due to short-range van der Waals forces.

The same butterfly-wing sample used in the confocal section is analyzed using the AFM. Unlike the SEM sample, this sample has no sputter coating since the AFM does not require any specific sample preparation. The AFM is equipped with an Antimony (n) doped Si tip with resonance frequency f_o: $313 - 370\ kHz$ and spring constant k: $20 - 80 \frac{N}{m}$.

Once the AFM has been calibrated for a specific tip and has its z-height focused, it is ready to scan a sample. For the installed tip, the machine finds the optimal frequency $348\ kHz$ with an oscillation setpoint of $231.9\ mV$. The integral and proportional gain parameters are set to 7 and 5 respectively, so the feedback loop may sufficiently react to the butterfly-wing sample which has many complex contours and height variation. A relatively flat sample would be best suited with lower gain values.

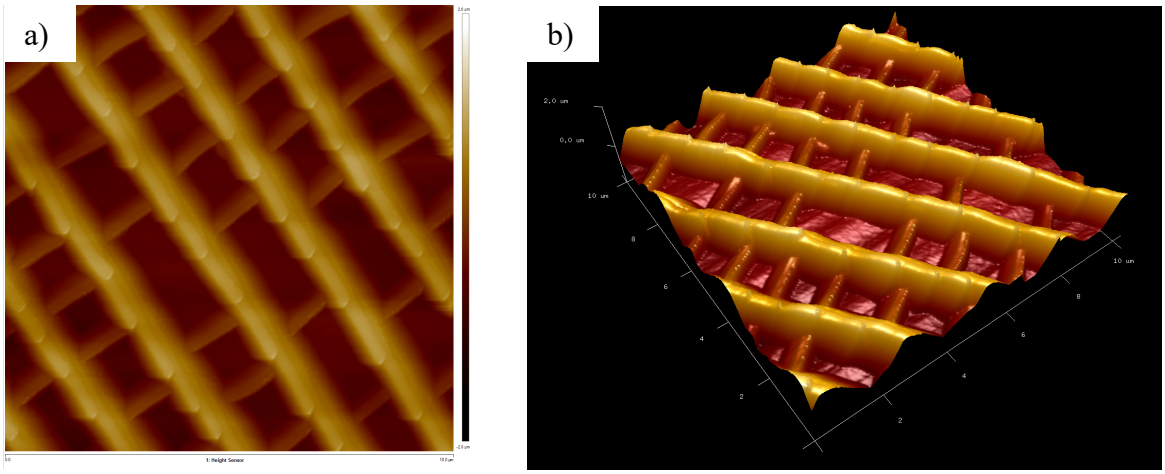

Figure 17: AFM scans of a butterfly wing sample with a scan-size of $10\mu m$ *and tip velocity of* $20\frac{\mu m}{s}$*. (a) Pseudocolor 2D height map of the wing's surface. (b) 3D reconstruction of the wing surface, pseudocolor-coded for height.*

Fig. (17) presents the AFM scans of the butterfly-wing's surface, with a size of $10\mu m \times 10\mu m$. This is a much smaller scale compared to the confocal scans in Fig. (1) and Fig. (3), yet the AFM still maintains high precision. Unlike the SEM images which are roughly at a similar scale, the AFM produces a true topographic height map: lighter colors indicate regions with a higher height, compared to darker colors which indicate regions of lower height. This height map and corresponding 2D view corroborate with the previous conclusions about the structure of the butterfly wing. The splines that ran vertically across the scales, providing structure, are here the light-yellow colored regions which protrude to the highest height in Fig. (17b). These splines appear to overlap one another in the 2D-view, and the 3D map demonstrates that there is only a minor height difference in the layers along the length of a spline. The highest splines protrude approximately $3 - 4\mu m$ from the body of the wing. The intermittent horizontal cross-hatching splines are seen at an intermediate height in this view around $0\mu m$ in the given scale. These minor splines appear to be at a consistent height halfway between the base of the scale and the major splines, and they are arranged perpendicular to the major splines. The main body of the scale, at the lowest height, is not perfectly flat: Fig. (17b) indicates that it has a slightly inconsistent and rough texture with height variations.

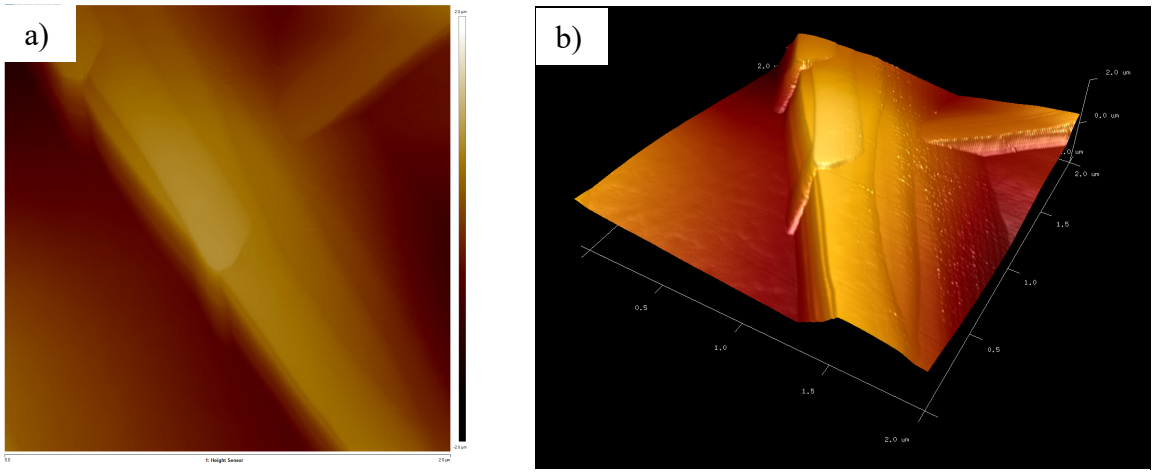

Figure 18: AFM scans of a butterfly wing sample with a scan-size of $2\mu m$ *and tip velocity of* $4\frac{\mu m}{s}$*. (a) Pseudocolor 2D height map of the wing's surface. (b) 3D reconstruction of the wing surface, pseudocolor-coded for height.*

Fig. (18) presents an even smaller AFM scan of the wing's surface, this time with a size of $2\mu m \times 2\mu m$. This view displays the topography of the major-splines on the butterfly-wing in detail. In the 2D-view in Fig. (18a), the spline is comprised of very thin layers stacked upon one another. The NanoScope software also allows for surface-roughness measurement from the AFM scan. The individual layers of the spline appear quite smooth, with a measured surface roughness of $6.63\ nm$ in the target region displayed in Fig. (19). Fig. (18b) corroborates this, also displaying how the spline has a steep edge on the left where the individual layers may be made out. The other side of the spline slopes downwards to the body of the scale; the minor cross-hatched spline intersects the major-spline around $2\mu m$ below the major-spline's maximum height. Again, the major spline rises to about $3\mu m$ above the base of the scale. The minor spline appears to have jagged artifacts along its length, likely due to the probe's finite scanning resolution. The sloped transition between the major spline and the base of the scale appears to have the roughest texture observed in these AFM scans.

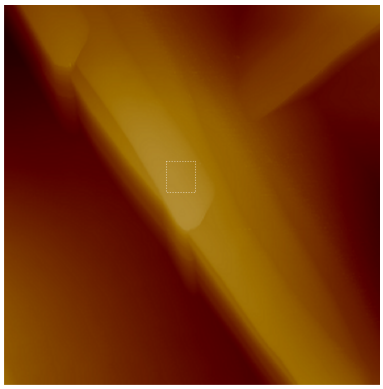

Figure 19: A repeated view of the $2\mu m$ AFM 2D height map from Fig. (18a) with a $0.149\mu m \times 0.157\mu m$ region selected for surface roughness measurement.

For reference, the amplitude error and phase images from the $2\mu m$ scan are displayed in Fig. (20). These images do not illuminate any particularly interesting information for the butterfly wing sample, but they can often be useful in multi-phase or other more complex samples to reveal further details about the sample. The amplitude error image captures discrepancies between the probe's setpoint and its actual amplitude, highlighting edge regions and regions of rapid change in height. There is highest magnitude (error) at the edge of the splines on the butterfly scale, while the base region is almost entirely uniform. The phase image portrays differences between the cantilever's driven and actual phase, typically providing contrast related to compositional changes of a sample, although not entirely relevant here.

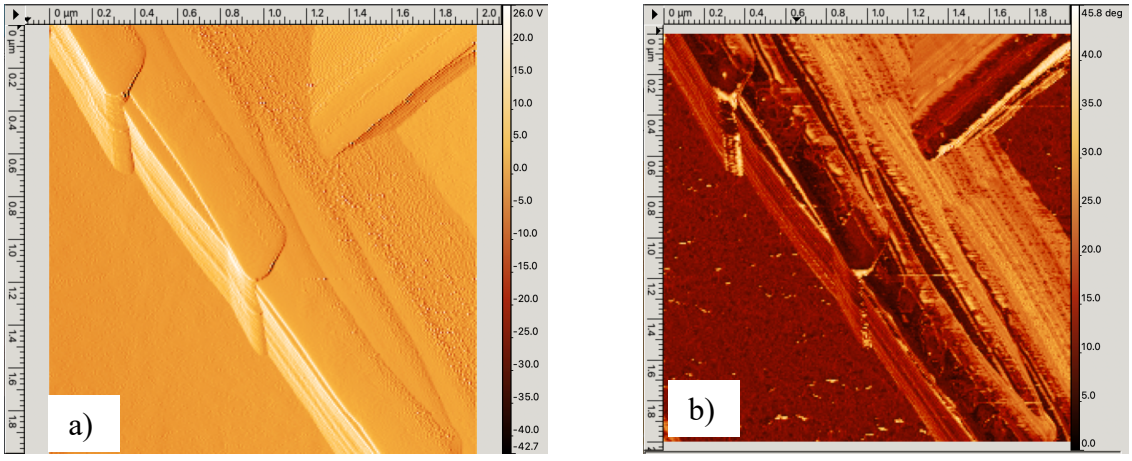

Figure 20: Further analysis of the $2\mu m$ AFM scan of the butterfly-wing sample from Fig. (18). (a) The pseudocolor-coded amplitude error image where the magnitude represents the error in the feedback loop controlling the AFM probe's height. (b) The pseudocolor-coded phase image where the magnitude represents the phase mismatch between the driven and actual frequency of the AFM probe.

Thus, AFM is an extremely powerful technique to capture and analyze the topography and other nanoscale properties of a sample, producing beautiful images with little sample preparation.